

Water-Vapor Absorption Database using Dual Comb Spectroscopy from 300-1300 K Part II: Air-Broadened H₂O, 6600 to 7650 cm⁻¹

Scott C. Egbert¹, Keeyoon Sung², Sean C. Coburn¹, Brian J. Drouin², Gregory B. Rieker¹

1 – Precision Laser Diagnostics Laboratory, University of Colorado, Boulder

2 – Jet Propulsion Laboratory, California Institute of Technology

© 2024. All rights reserved.

Abstract

We present broadband dual frequency comb laser absorption measurements of 2% H₂O (natural isotopic abundance of 99.7% H₂¹⁶O) in air from 6600-7650 cm⁻¹ (1307-1515 nm) with a spectral point spacing of 0.0068 cm⁻¹. Twenty-nine datasets were collected at temperatures between 300 and 1300 K ($\pm 0.82\%$ average uncertainty) and pressures ranging from 20 to 600 Torr ($\pm 0.25\%$) with an average residual absorbance noise of 8.0E-4 across the spectrum for all measurements. We fit measurements using a quadratic speed-dependent Voigt profile to determine 7088 absorption parameters for 3366 individual transitions found in HITRAN2020. These measurements build on the line strength, line center, self-broadening, and self-shift parameters determined in the Part I companion of this work. Here we measure air-broadened width (with temperature- and speed-dependence) and air pressure shift (with temperature-dependence) parameters. Various trends are explored for extrapolation to weak transitions that were not covered in this work. Improvements made in this work are predominantly due to the inclusion of air pressure shift temperature dependence values. In aggregate, these updates improved RMS absorbance error by a factor of 4.2 on average, and the remaining residual is predominantly spectral noise. This updated database improves high-temperature spectroscopic knowledge across the 6600-7650 cm⁻¹ region of H₂O absorption.

Introduction

H₂O vapor is a strong absorber of infrared radiation and is found in a host of combustion, atmospheric, and biological systems. Accurate characterization of H₂O vapor absorption, particularly when mixed with air, is crucial for understanding terrestrial radiative processes [1], [2], interpreting spectra from exoplanetary atmospheres [3], [4], and making non-intrusive combustion measurements [5], [6], [7], among a host of other applications. By comparing spectrally resolved absorption measurements against molecular absorption models, it is possible to determine the environmental conditions. For example, because H₂O is an abundant product of hydrocarbon combustion, near-infrared H₂O absorption is commonly used to measure thermodynamics parameters such as temperature [5], [6], [7], [8], [9], [10], [11], [12], concentration [5], [6], [7], [8], [9], [10], [11], [12], pressure [5], velocity [5], [11], [12], and even mass flux [5] in high-temperature reacting systems.

For molecules with discrete absorption transitions, such as H₂O, generating accurate, tabulated line-by-line absorption models hinges on two crucial elements: (1) the parametrization of the line shape model to account for the relevant molecular physics under the specific measurement conditions, which includes factors like collisional narrowing, foreign broadening, and temperature dependence, and (2) the tabulation of parameters within a comprehensive database, enabling model calculations across a spectrum of conditions. The failure to adequately address either of these aspects results in an erroneous spectral model and inaccurate calculations.

As described in Part I of this work [13], leading spectral parameter databases, such as HITRAN [14], HITEMP [15], ExoMol [16], and GEISA [17] include tens to hundreds of thousands of well-curated individual absorption transitions. Currently, these databases all employ a Voigt profile (VP) to represent the line shape of air-broadened H₂O absorption in the spectral region of interest. With improving measurement techniques and instrumentation, it has become increasingly evident that the VP model inadequately captures the true absorption line shape of H₂O, especially at elevated temperatures [18], [19], [20], [21], [22]. An alternative approach, the Partially-Correlated

Quadratic-Speed-Dependent Hard-Collision (pCqSDHC) model, demonstrates close agreement with high-resolution measurements [20]. At a fraction of the computational cost of the pCqSDHC model, augmenting the VP with quadratic speed dependence (SD) to create the SDVP model has been shown to match the signal-to-noise levels of many measurements [18], [19], [21].

In addition to identifying an appropriate line shape model, many parameters change as a function of temperature, including collisional narrowing and transition center frequency. While research into the temperature dependence of spectral shifts is ongoing, none of the databases described include parameters describing the temperature dependence (TD) of the shift in center frequency. Including this TD parameter was recently shown to reduce Doppler-shift-based velocity errors from 18% using the HITRAN database to 2% using the database presented in this work.

In Part I of this study [13], we updated line centers, line strengths, self-width, and self-shift parameters (with TD and SD of the width) contained in the HITRAN2020 database using 29 measurements spanning the same measurement region. Using these measurements, we updated 17030 absorption parameters for 5986 transitions and identified 574 features not presently catalogued in the database. Building on this updated H₂O database, here we use an additional 29 dual comb spectroscopy (DCS) measurements of absorption of 2% H₂O in air to update the foreign broadening and shift parameters of that same database. These measurements also span 6600 to 7650 cm⁻¹ with temperatures ranging from 300 to 1300 K and pressures from 20 to 600 Torr. In this study we measure 7088 absorption parameters for 3366 transitions, updating parameters for air-broadened and shifted H₂O (similarly with TD and SD of the width).

Overall, we see an improvement in RMS residual noise from 0.0025 to 0.0006, averaging across all measurements, with the improvement originating from updates to a balance of both the broadening and shift parameters. The remaining residual is largely due to spectral noise with a small residual due to the TD of SD parameters for the largest features. After computing values for the SDVP database, we removed SD and re-optimized the parameters for use when the Signal-to-Noise Ratio (SNR) or computational bandwidth only requires the VP.

This work is the only broadband (hundreds of cm⁻¹), high-temperature (over 1000 K), experimentally derived air-broadened H₂O database known to the authors. Together with the foundation derived from the pure H₂O measurements in Part I, this work presents an empirically-validated H₂O database optimized for high-temperature combustion and exoplanetary measurements in the presence of air.

Experimental Setup

Spectrometer

As described in Part I of this work [13], Dual Comb Spectroscopy (DCS) is a promising technique well-suited for high-temperature database applications. It combines several advantageous characteristics of traditional Fourier Transform Spectroscopy (FTS) and Tunable Diode Laser Absorption Spectroscopy (TDLAS). Much like FTS, DCS can capture wide spectra spanning over 1000 cm⁻¹ while maintaining high resolution for individual absorption transitions at terrestrial conditions (less than 0.1 cm⁻¹). Like TDLAS, DCS utilizes an actively modulated laser light source, effectively isolating the absorption measurement from background radiation due to thermal emission – a concern that can compromise the performance of FTS in high-temperature environments.

Our DCS system [13], [23], [24] consists of two mode-locked frequency comb lasers operating at slightly different repetition rates ($f_r = 204$ MHz, $\Delta f_r = 436$ Hz), fully phase locked for continuous coherent averaging [25], [26], [27]. Measurements for Parts I and II of this work were taken concurrently using the same optical setup and spectrometer. We lock one comb tooth from each laser to a narrow linewidth Continuous Wave (CW) reference laser (1.5 kHz linewidth RIO Planex) at 1565 nm, resulting in comb tooth linewidths on the order of tens of kHz [28]. Comparable to [13], the precision of the frequency axis was primarily influenced by the stability of the CW laser, exhibiting a sinusoidal fluctuation with an amplitude of ± 5 Hz (50 ppb out of 204 MHz), thus introducing an estimated frequency axis uncertainty of $1.74\text{E-}4$ cm⁻¹ [23]. We actively reference all frequency measurements to a

GPS-disciplined quartz oscillator (Jackson Labs Fury) with 10 ppt stability, contributing negligible frequency drift in comparison to other sources of uncertainty.

The laser pulses generated by each comb are individually amplified and spectrally broadened to include hundreds of thousands of comb modes (wavelengths), spanning the range of 1.3-1.8 μm , evenly spaced at the laser repetition rate (204 MHz or 0.0067 cm^{-1}). We then spectrally filter this light to $6600\text{-}7650\text{ cm}^{-1}$ using an optical lens and diffraction grating. A slight detuning of the frequency comb repetition rates ($\Delta f_r = 436\text{ Hz}$), gives a unique frequency offset to each successive pair of comb modes. We use a detector to measure the heterodyne beats (interferogram) between the lasers where the RF frequencies present in the interferogram (sampled from 0-100 MHz) correspond to the comb mode pairs of the dual-comb lasers. The amplitude of each measured RF frequency indicates the transmission (or attenuation) of the laser at the corresponding infrared frequency. This process transforms the THz infrared frequencies of successive pairs of comb modes into MHz frequency beats, directly proportional to the magnitude of these comb mode pairs [27], [29]. Like Cole [23], we were careful to avoid measurement distortions due to phase noise [30], detector linearity [31], and cross-phase modulation [32].

Recent advancements in DCS measurements [33] demonstrated a sub-0.1% precision in atmospheric O_2 concentration measurements by including a voltage dither with the interferogram signal before digitization. This dither randomized interferogram data points across numerous digitization registers, reducing any potential bias stemming from excessive reliance on registers near the average voltage. Employing the same technique in this study, we applied a 1 MHz, 100 mV_{pp} dither to the detector output before digitization. Notably, no digital filtering was necessary to eliminate the dither signal, as the 1 MHz frequency corresponds to the heterodyne beat note that emerged between comb teeth at 6450 cm^{-1} , a region outside the measurement range for this work. Interferograms for each measurement condition were meticulously phase-corrected and coherently averaged over approximately one hour, yielding an average absorbance noise level of $8.0\text{E-}4$ across the entire spectrum for all conditions under investigation, comparable to the $7.4\text{E-}4$ absorbance noise from Part I [13].

Furnace and Spectroscopy Cell

In Figure 1, we present a schematic of the high-temperature optical cell used in this study. This is the same setup we presented in Part I [13], with the addition of a mixing tank to hold a consistent, pre-mixed charge of air-water gas. The optical setup consists of a 45.7 cm quartz static-sample cell inside of a purged quartz tube at the center of a 106 cm long furnace (CM Furnace) with three independent temperature zones. We double-passed the DCS laser beam along the upper region of the spectroscopy cell, resulting in a cumulative absorbing pathlength of $91.4 \pm 0.1\text{ cm}$. This extended optical pathlength enables us to detect and analyze a multitude of weakly absorbing features, especially at the lower number densities observed at elevated temperatures.

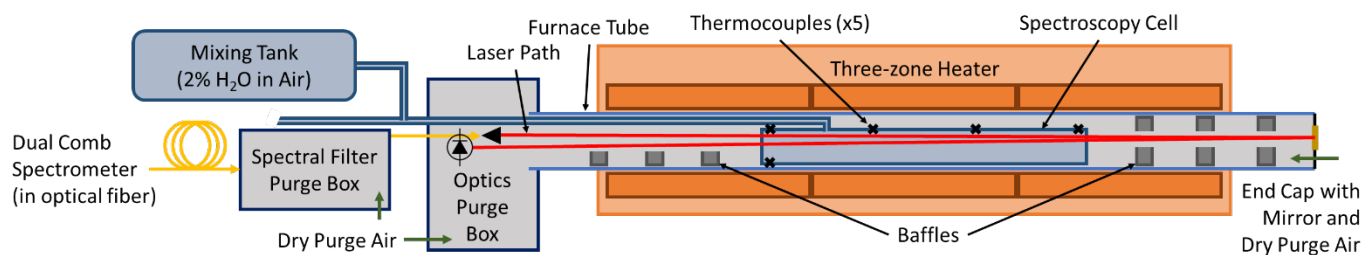


Figure 1: Schematic of the high-temperature furnace used for data collection in [13] and this work. A 45.7 cm spectroscopy cell is centered in a 106 cm three-zone furnace. Baffles were used to reduce convective currents and improve axial temperature uniformity. The 3 cm diameter absorption cell was placed in a 9 cm diameter, 165 cm long quartz tube that was capped at one end and enclosed at the other to allow all free space optics to be purged of background H_2O absorption. The DCS laser beam was passed through a purged spectral filter before being passed twice through the furnace for an effective pathlength of 91.4 cm. A 12 L mixing tank was used to give a consistent mixture of air and H_2O for each measurement.

To mitigate temperature variations arising from convection, baffles were strategically placed at the furnace's periphery. Whenever experimental conditions were altered, the furnace temperature was allowed to stabilize for a

minimum of 3 hours. Additionally, a continuous flow of dry air was employed to reduce and stabilize the moisture content from ambient air in the furnace and the grating-based spectral filter.

We measured temperature of the absorption cell in five locations using k-type thermocouples (Omega): four axial positions along the upper section of the spectroscopy cell, positioned closest to the laser beam's path, and an additional radial measurement at the cell's lower section to assess radial temperature variations. Our reported temperature uncertainty includes instrument, temporal, axial, and radial variations, added in quadrature. On average, the temperature uncertainty was 0.82% relative to the measurement value, with a maximum uncertainty of 1.54% at 1300 K. The dominant source of uncertainty at lower temperatures is the thermocouple measurement uncertainty itself, and at higher temperature, axial non-uniformity. Temporal and radial variations remained negligible across all experimental conditions.

Comparable to the companion study presented in Part I [13], high purity, vacuum degassed H₂O (Honeywell CAS 7732-18-5) of natural isotopic abundance (99.7% H₂¹⁶O) was used for each measurement. For this work, the H₂O was pre-mixed with synthetic air (Airgas Ultra Zero, less than 2ppm of H₂O and 1ppm of CO₂+CO) in a stainless-steel mixing tank (12 L) before being measured in the furnace. When preparing a sample, we filled this tank to 17 Torr of pure H₂O ($P_{sat,295K} = 19$ Torr) before pressurizing to 850 Torr using the synthetic air, targeting a concentration of 2% H₂O in air. We then agitated the stainless-steel ball bearings that had been placed in the tank for 15 minutes to thoroughly mix the air and water before leaving the mixture to fully equilibrate for at least 12 hours before use. Two batches of air-water mixture were used to complete all measurements: one for all 300 and 500 K measurements and a second for 700, 900, 1100, and 1300 K measurements.

Before each measurement, we first flushed the absorption cell down to tens of mTorr, filled it to near the measurement pressure using a fresh charge of air-water mixture, allowed this mixture to sit for nominally five minutes, emptied the cell again, and then filled the cell to the desired pressure for the measurement condition. We used this process to equilibrate the H₂O adsorption in the stainless-steel tubing, stabilizing the water concentration for each measurement. DCS measurements were taken after the total pressure stabilized, indicating the H₂O was in equilibrium with the stainless-steel, a process that took nominally five minutes after filling the absorption cell.

Pressure in the spectroscopy cell was continually monitored using a 1000 Torr Baratron capacitance manometer (MKS-628D) with an uncertainty of 0.25% of the measured value that was calibrated (NCSL Z540.1) immediately prior to data collection. Our reported pressure uncertainty consists of both temporal and instrument uncertainties added in quadrature, averaging 0.25% for all measurements with a max of 0.26% due to minor temporal fluctuations at 1100 K, 40 Torr. The leak rate of the 2-liter absorption cell volume was negligible at less than 0.1 mTorr per hour over a 60-hour test below 10 mTorr. We actively evacuated the spectroscopy cell overnight before each day of data collection to fully remove H₂O vapor from the cell and tubing. A background measurement was then taken before adding H₂O to the cell to characterize the shape of the laser baseline and to quantify background H₂O absorption from the air in the spectral filter and outside of the absorption cell in the furnace.

The test matrix summarizing conditions and respective uncertainties for all measurements is shown in Table 1. In total, 29 spectra were taken, with at least five different pressure measurements at each of five temperatures. Only one measurement (600 Torr) was collected at 1300 K to reduce damage to the quartz from prolonged exposure to H₂O vapor at high temperatures. Additional low-temperature measurements were taken to better characterize strong absorbing features that saturate at lower temperatures and higher pressures (i.e. 8 features at 300 K and 300 Torr have transmission below 15%).

Table 1: Average conditions measured for this work. Temperature uncertainty is dominated by thermocouple instrument uncertainty at low temperatures and a mix of thermocouple and axial uniformity at elevated temperatures. Pressure uncertainty is dominated by pressure gage instrument uncertainty. Additional room temperature measurements were taken at lower pressures to better characterize strongly absorbing features. Only one measurement at 1300 K was taken to avoid quartz/water vapor exposure damage.

Temperature (K)	Pressure (Torr)
295 ± 2	20.2±0.1, 40.3±0.1, 59.6±0.1, 80.0±0.2, 119.6±0.3, 159.7±0.4, 319.9±0.8, 599.5±1.5
505 ± 4	40.0±0.1, 79.6±0.2, 162.1±0.4, 320.8±0.8, 601.0±1.5
704 ± 5	40.0±0.1, 80.0±0.2, 160.2±0.4, 319.9±0.8, 599.9±1.5
901 ± 8	40.1±0.1, 80.2±0.2, 159.8±0.4, 319.3±0.8, 599.8±1.5
1099 ± 11	40.1±0.1, 80.2±0.2, 160.0±0.4, 319.8±0.8, 599.5±1.5
1288 ± 20	599.4±1.5

We optically calculated H₂O concentration for each measurement using the measured absorption from a combination of 225 isolated features and 26 isolated doublet pairs, all of which were visible and unambiguously isolated from other absorption transitions at all measurement conditions. An SDVP (foreign width with TD, foreign shift with TD, and SD of the foreign width) was fit to each of the features with sufficient SNR, or feature pairs, at every condition using the line strength, center, and self-SDVP values calculated in Part I [13]. We then averaged the concentrations for all 251 features to obtain the H₂O concentration at that measurement condition, as shown in Figure 2. Due to the 60x variation in number density across measurements, not all features were visible at all measurements conditions. As such, only features with less than 10% uncertainty were included in the average, with the 300 K, 20 Torr condition using the fewest (220 absorption features). We estimate H₂O concentration uncertainty as the standard deviation between the concentrations from each of the up to 251 measured features (averaging 2.9% relative to the concentration) and the relative temperature, pressure, and pathlength uncertainty for each measurement, added in quadrature.

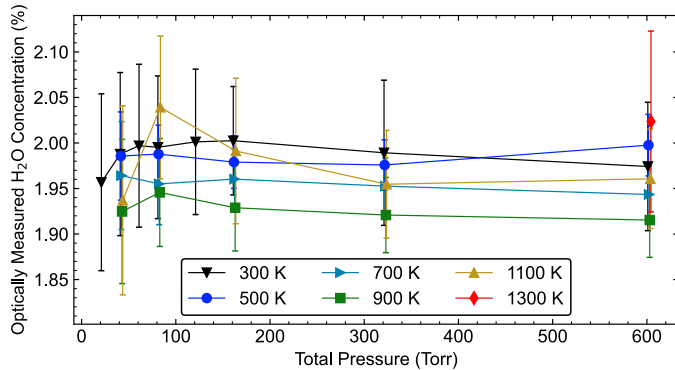


Figure 2: Optically calculated H₂O concentration for each measurement condition (see Table 1), calculated by averaging the concentration obtained from between 220 and 251 isolated absorption features, depending on feature SNR at each condition. Uncertainty sources include fit, temperature, pressure, and pathlength and average 3.1% relative to the concentration.

Data Preparation

In this work, we employed the same methodology for processing DCS measurements as presented in Part I [13] and shown in Figure 3 of this work. A series of scans with the optical cell at vacuum conditions were taken each day of testing to both characterize the spectral shape of the laser baseline and to quantify the background water concentration. The raw vacuum scan associated with the 1300 K furnace temperature is shown in the top row of Figure 3 in panels A and B in orange. A two-temperature spectral model was fit to each vacuum scan to quantify high-temperature absorption in the furnace and low-temperature absorption in the spectral filter (see Figure 1). This absorption was then subtracted from the vacuum scan to isolate the laser baseline (teal) before the baseline was low-pass filtered to remove noise and isolate the laser shape (black). As in Part I, the average background H₂O concentration we observed was 292 ppm with variations on the order of 31 ppm between vacuum scans at different conditions.

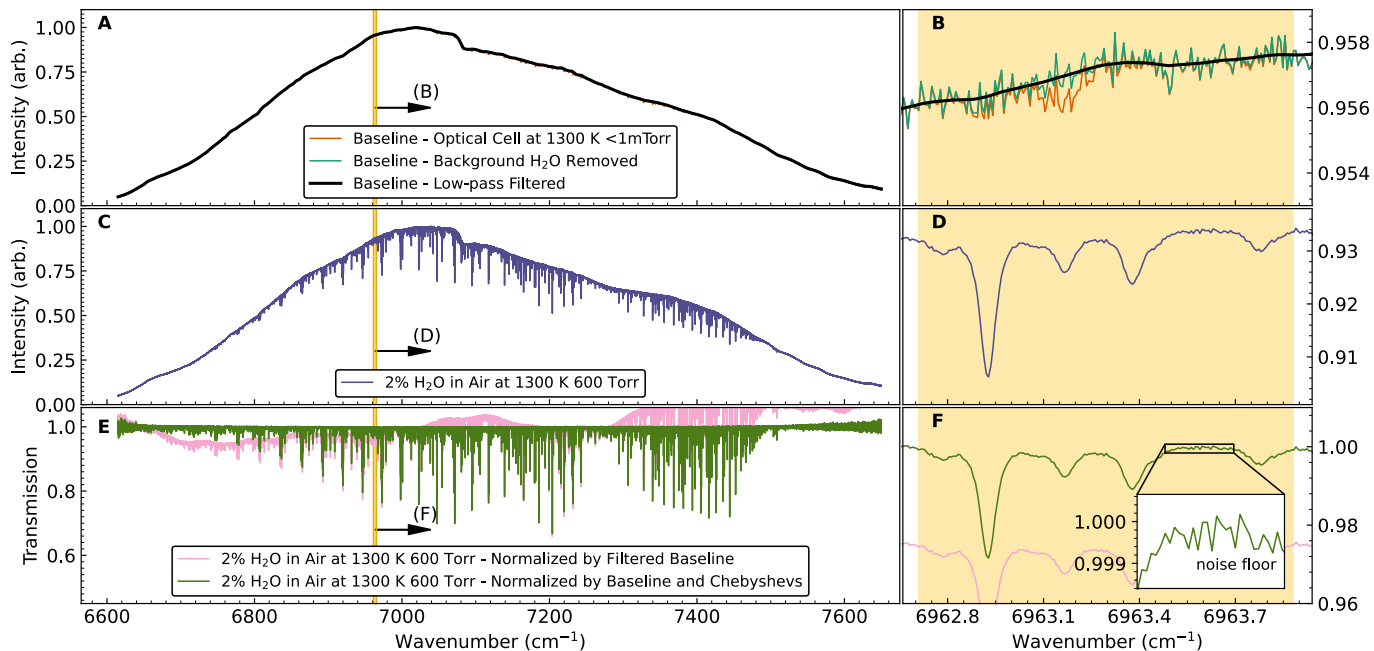


Figure 3: Measurements and data processing used to prepare transmission data for this work. Panels A and B show the background measurements taken with the sample cell under vacuum to characterize background H₂O absorption (orange), the background scan with molecular absorption quantified and removed (teal), and a smoothed laser transmission baseline (black). Panels C and D show the 1300 K, 600 Torr measurement of 2% H₂O in air (purple). Panels E and F show the same measurement normalized by the smoothed baseline (pink). Additional normalization due to large-scale fluctuations in laser baseline was performed using a 7th order Chebyshev across overlapping 25 cm⁻¹ segments to fully normalize the spectrum (green). The inset in panel F highlights the noise floor of the measurement at right (7.5E-4 for the measurement at this condition, slightly below the 8.0E-4 average for all measurements).

Panels C and D of Figure 3 show the raw measurement as obtained from the DCS at 1300 K and 600 Torr with the comparable laser baseline to the vacuum scan (panel A) clearly visible. We divided the raw measurements by the smoothed vacuum scan to obtain the partially normalized spectrum shown in pink in panels E and F, where the low-frequency oscillations are due to small fluctuations in the laser intensity over time and do not impact individual features. Background H₂O absorption from H₂O outside of the spectroscopy cell, as calculated from the vacuum scan, was then subtracted from the measured absorbance. Returning to transmission, during the fitting routine we used 7th-order Chebyshev polynomials across 25 cm⁻¹ segments of the spectrum to normalize for the remaining low-frequency oscillations, resulting in the green trace presented in Panels E and F. Panel F includes an inset to highlight the measurement noise floor of 7.5E-4 absorbance noise for this specific measurement and 8.0±2.6E-4 for all the measurements in our study. On the left side of this inset, you can observe the distant wings of the feature at 6963.4 cm⁻¹.

We excluded data points below the conservative cutoff of 15% transmission from the fitting algorithm due to the high uncertainties associated with high-absorbance/low-transmission data points and the absence of DCS validation under these conditions. For this work, only features at 300 K were affected with 8 features exhibiting high absorbance at 600 Torr, 7 at 320 Torr, 5 at 160 Torr, and 3 at 120 Torr. Because these features absorb light so strongly, they still have excellent SNR in lower pressure measurements. This deliberate choice to omit a few well-documented, low-temperature features at high pressure (rather than limiting the number density of H₂O vapor to avoid high absorbance) enabled us to focus on measuring thousands of high-temperature features, aligning with the primary objective of this research.

Line Shape Model and Multispectrum Fitting

Line Shape Model

Line shape models are used to reduce measured spectra into a set of line-by-line absorption model parameters that can be used to predict absorption at a range of conditions. Our dataset includes thousands of individual absorption features with SNR varying by over three orders of magnitude over the noise floor of the measurement. To effectively analyze such a large number of features of different SNR, we applied the multispectrum fitting algorithm initially introduced in [34], a method that has consistently demonstrated its capability to accurately retrieve hundreds of line shape parameters using high-resolution spectra (such as [13], [23], [24], [35], [36], [37]). In multispectrum fitting, all measurements are fit simultaneously to calculate the best values for each parameter. The ability to determine up to five parameters for hundreds of transitions at a time was essential for processing these broadband measurements in a reasonable timeframe and will be described in greater detail in the following section. When reducing spectral measurements into modeled parameters, we used the quadratic speed-dependent (SD) Rautian profile, as defined in Equation 1:

$$F(x, y, a_w, H) = \frac{2}{\pi^{3/2}} \int_{-\infty}^{+\infty} v e^{-v^2} \arctan \left(\frac{x(T, P) + v}{y(T, P) \left(1 + a_w \left(v^2 - \frac{3}{2} \right) \right) + H} \right) dv \quad (1)$$

Where the dimensionless line shape profile, F , is a function of the dimensionless center frequency, x , Lorentz width, y , and Dicke narrowing coefficient, H [13], [35]. The dimensionless SD parameter, a_w , is the ratio of the SD and collisional (Lorentz) broadening. Collisions are normalized by the most probable speed for a given temperature, which was calculated from $v = -4$ to 4 in 16 steps at each frequency of the transition [35]. Previous analysis has found that SD dominates Dicke narrowing at the temperatures and pressures measured in this work [21], [22], comparable to Part I [13]. Because the matrix-based solver [34] is not designed to simultaneously determine the highly coupled SD and Dicke narrowing, only SD values were analyzed for this study with H set equal to zero, reducing the SD Rautian profile to the SD Voigt Profile (SDVP). Additionally, due to the low concentration of H₂O in this work, air-H₂O SD is the dominant form of SD narrowing. H₂O-H₂O SD calculations performed in part I were not included in this study due to limitations of the matrix-based solver.

For an absorbing molecule in air, the dimensionless line center parameter, x , from Equation 1 is parameterized as shown in Equation 2:

$$x(T, P) = \frac{\sqrt{\ln(2)}}{\gamma_{Doppler}} (\sigma - \sigma_0 - P[X_{self}\delta_{self}(T) + X_{air}\delta_{air}(T)]) \quad (2)$$

Where σ is the frequency at which the lineshape is to be determined, σ_0 is the center frequency of the transition at vacuum, P is the gas pressure, X_{self} is the concentration of the absorbing molecule, δ_{self} is the collisional self-shift at the gas temperature, T , X_{air} and δ_{air} are the concentration of air and corresponding air pressure shift, and $\gamma_{Doppler}$ is the Doppler width of the transition [35]. Similarly, the parameterization for the dimensionless line width parameter, y , is shown below in Equation 3:

$$y(T, P) = \frac{\sqrt{\ln(2)}}{\gamma_{Doppler}} P[X_{self}\gamma_{self}(T) + X_{air}\gamma_{air}(T)] \quad (3)$$

Where γ_{self} is the Lorentz self-width and γ_{air} is the air-width at the gas temperature. For both Equations 2 and 3, describing the variation of δ_{self} , δ_{air} , γ_{self} , and γ_{air} with temperature is a non-trivial subject of continued investigation and will be discussed in detail in the following sections.

Multispectrum Fitting Procedure

We employed a comprehensive multispectrum fitting approach, utilizing all acquired data collectively to extract optimal fits for each feature under diverse conditions [34]. To accelerate each processing iteration, we partitioned the spectral data into 58 segments averaging $20 \pm 2 \text{ cm}^{-1}$ wide, excluding regions with sparse H_2O absorption near 6600 and 7650 cm^{-1} , comparable to part I [13]. We tailored these bin widths to ensure complete isolation of spectral features within each bin. Recognizing the potential slow drift in laser intensity between vacuum and measurement scans, we employed an additional baseline normalization strategy for each bin using 7th order Chebyshev polynomials, adding an extra 2 cm^{-1} buffer on both sides of each bin to mitigate edge-related artifacts. A 7th order Chebyshev polynomial spanning nominally 24 cm^{-1} had negligible impact on spectral features, which exhibited a maximum width on the order of 1.2 cm^{-1} for the largest of overlapping features.

As discussed in Part I of this work for pure H_2O , identifying how the spectral widths and shifts shown in Equations 2 and 3 change with temperature is an essential part of an accurate spectroscopic database. Furthermore, when measuring molecules with congested absorption spectra, as is the case for air-broadened H_2O in this region, appropriate TD relationships can help discriminate among overlapping transitions by combining information from measurements at multiple temperatures.

The single power law (SPL) relationship, as shown in Equations 4 and 5 for the air-broadened Lorentz width and air pressure shift, is a common TD parameterization that was used in this multispectrum fitting routine, comparable to the measurements presented in Part I of this work for self-widths and shifts.

$$\gamma_{air}(T) = \gamma_{air}^0 \left(\frac{T_{ref}}{T} \right)^{n_{\gamma,air}} \quad (4)$$

$$\delta_{air}(T) = \delta_{air}^0 \left(\frac{T_{ref}}{T} \right)^{n_{\delta,air}} \quad (5)$$

Here, $\gamma_{air}(T)$ is the observed Lorentz width due to collisions between the absorbing molecule and air at the gas temperature, T , as shown in Equation 3. γ_{air}^0 is the air-broadened half-width at the reference temperature, T_{ref} , and $n_{\gamma,air}$ is the SPL TD exponent. In Equation 5, $\delta_{air}(T)$ is the collisional air pressure shift, δ_{air}^0 is the air pressure shift at the reference temperature, and $n_{\delta,air}$ is the SPL TD exponent.

A Double Power Law (DPL) model, where two sets of the SPL TD model are added together, was proposed by Gamache and Vispoel [38] and explored by Stolarczyk et al. [39] where it showed good agreement to theoretical calculations of H_2O widths and shifts over broad temperature ranges, such as $100\text{-}3000 \text{ K}$. Due to limitations inherent to processing thousands of transitions that are often only visible at a subset of the six measured temperatures, the four parameter DPL model has not been integrated into the multispectrum fitting routine used in this work. The impact of using SPL TD for widths and shifts will be explored in greater detail in the next section.

To estimate initial values for a_w , we analyzed 127 isolated transitions where statistical fit uncertainties for a_w and $n_{\gamma,air}$ were below ± 0.007 while floating other width and shift parameters and found an average value for of a_w 0.130 ± 0.022 . While we will show in the Results and Discussion that a_w is not as constant for H_2O -air collisions as was found in Part I for H_2O - H_2O collisions, 0.13 was used as an initial estimate for a_w due to the lack of a_w parameters in the HITRAN database. In this analysis of the most isolated features, we did not find notable trends in $n_{\delta,air}$ that could be reliably extrapolated to initial values and instead chose to set initial values of all $n_{\delta,air}$ parameters to 1 (proportional to P/T).

Our work is built on the database we developed in Part I using measurements of pure H₂O [13]. In that work, we calculated line strengths, centers, self-widths, and self-shifts using a similar procedure to what we used for the air-H₂O measurements. We use a similar, systematic processing procedure to obtain comparable results across the 1050 cm⁻¹ wide spectrum by establishing an upper limit for statistical uncertainties for each parameter. For each spectral feature, we incrementally float additional parameters until the predetermined uncertainty limit is no longer met for all of the evaluated parameters associated with that feature, iterating ten times to ensure stable convergence. The sequential steps used in this work are outlined below:

1. We floated parameters to minimize a large residual that could disrupt calculations for nearby features, typically width parameters of larger features, although occasionally spectral shifts.
2. Width parameters were then floated for all features above the measurement noise floor, beginning with γ_{air}^0 , then $n_{\gamma,air}$, and finally a_w . Parameters that could not be determined to within ± 0.12 , ± 0.13 , and ± 0.10 , respectively for γ_{air}^0 , $n_{\gamma,air}$, and a_w were only floated if the updated value stably reduced model residuals and were evaluated on a case-by-case basis.
3. Finally, shift parameters were floated for features meeting all prior uncertainty limits. Uncertainty limits for δ_{air}^0 and $n_{\delta,air}$ were ± 0.005 cm⁻¹ and ± 0.13 , respectively.

We repeated this operation for all 58 bins across the 1050 cm⁻¹ measurement range. In some instances, features overlapped in a way that prevented us from identifying unique parameters for the underlying transitions at the conditions measured. Work by Toth and Brown have identified families of features based on quantum assignment that share width coefficients [40], [41]. Like Schroeder et al. [36] and Part I of this work [13], we constrained the width coefficients (γ_{air} , $n_{\gamma,air}$, and $a_{w,air}$) of doublet pairs to be equivalent. We did not constrain shift relationships (δ_{air} and $n_{\delta,air}$) due to the ambiguous relationship between doublet pairs.

Temperature Dependence Model

In this section we will first describe common TD parameterizations as alternatives to the Single Power Law (SPL) and then present measurements of γ_{air} and δ_{air} as a function of temperature for isolated transitions to explore the limitations and benefits of the SPL model used for in the multispectrum fits presented in this work. This parallels analysis performed in Part I for pure H₂O where the SPL TD was shown to fit the data to the noise floor of the measurement.

Due in part to the anharmonicity of H₂O, γ_{air} and δ_{air} can exhibit complicated behavior as a function of temperature. For δ_{air} in particular, this can include changes from positive to negative spectral shifts, which cannot be represented using SPL TD. Consequently, simple, linear TD models have also been explored to represent δ_{air} , as shown in Equation 6:

$$\delta_{air}(T) = \delta_{air}^0 + \delta'(T - T_{ref}) \quad (6)$$

Where δ' is the TD slope coefficient. While the linear TD model can represent changes in δ_{air} sign, it is not well suited to observed trends in TD and extrapolates poorly over temperature ranges as low as 100 K [39].

Recent analysis by Gamache and Vispoel [38] exploring higher fidelity parameterizations for γ_{air} and δ_{air} have presented a Double Power Law (DPL) TD relationship, as shown in Equations 7 and 8, to more accurately represent the expected TD at all gas temperatures.

$$\gamma_{air}(T) = \gamma_{air}^a \left(\frac{T_{ref}}{T}\right)^{n_{\gamma,air}^a} + \gamma_{air}^b \left(\frac{T_{ref}}{T}\right)^{n_{\gamma,air}^b} \quad (7)$$

$$\delta_{air}(T) = \delta_{air}^a \left(\frac{T_{ref}}{T}\right)^{n_{\delta,air}^a} + \delta_{air}^b \left(\frac{T_{ref}}{T}\right)^{n_{\delta,air}^b} \quad (8)$$

Where the combination of γ_{air}^a and γ_{air}^b , each with corresponding temperature dependencies $n_{\gamma,air}^a$ and $n_{\gamma,air}^b$, in Equation 7 are used to represent γ_{air} with more flexibility than SPL TD. Equation 8 allows for both positive and negative values of δ_{air} as a function of temperature.

The DPL is an extended model to capture the temperature dependence trends across broad temperature ranges, e.g. 0 - 3000 K, as shown for the theoretical calculations in [38], [39]. As was shown in Part I of this work, fitting DPL TD to finite measurements over a limited temperature range is challenging. With only six measured temperatures between 300-1300 K, it can be unclear if the four DPL parameters determined from these measurements are overfitting the measurement. Additionally, the vast majority of the 3366 observed transitions in this work are only present above the measurement noise floor in a subset of these six measured temperatures.

To better understand TD behavior for the measurements presented in this work, 221 out of the 3366 observed transitions were identified that are (1) present above the noise floor at all six measured temperatures and (2) have no neighboring transitions that contribute (interfere) meaningfully with the measured absorption at any of the measured temperatures. For these 221 transitions, γ_{air} , δ_{air} , and a_w were retrieved at each temperature using all measurements at that temperature (typically five pressures, with eight pressures at 300 K and one at 1300 K, see Table 1). This process was confirmed to fit the data to the noise floor of the measurement. Models calculated using the lineshape parameters from the multispectrum fitting routine described in the previous section as well as HITRAN data, where available, are also compared to these temperature specific retrievals.

Temperature specific parameters (left) and transmission data (right) for the $2\nu_2+\nu_3$ ($4_{2,2} \leftarrow 3_{2,1}$) transition are shown in Figure 4, where rotational quanta are listed using $J_{Ka,Kc}$ notation. Retrieved values for γ_{air} (panel A), δ_{air} (B), and a_w (C) are shown on the left, each as a function of temperature. The HITRAN prediction for γ_{air} (using SPL TD) is shown in panel A in red with the uncertainty shaded. A multispectrum fit of all measurements in this work (also using SPL TD) is shown in green, with a shaded uncertainty. A DPL TD model was fit to $\gamma_{air}(T)$, weighted by uncertainty, and is shown in blue. Similar results are shown in panels B and C for δ_{air} and a_w , respectively, noting that HITRAN does not include parameters for $n_{\delta,air}$ or SD. Measured transmission data for the highest pressure measured (600 Torr) is shown at the top right in panel D, with the residual of the measurement minus a model computed using the HITRAN database and the updated database from the MultiSpectrum Fit in This Work (MSF TW) on the lower right in panels E and F, respectively.

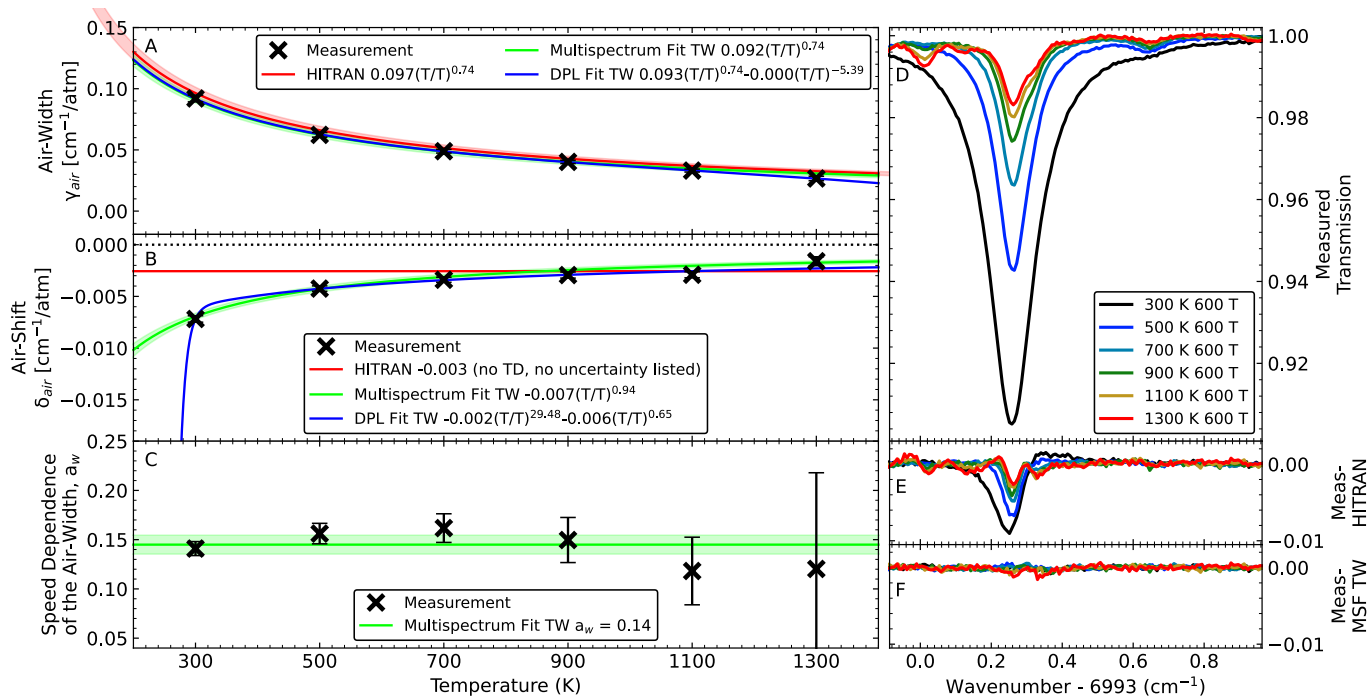


Figure 4: Left: γ_{air} (panel A), δ_{air} (B), and a_w (C) for the $2v_2 + v_3$ ($4_{2,2} \leftarrow 3_{2,1}$) transition as a function of temperature. Measured values at each temperature are shown in black, with database values from HITRAN2020 (red, no TD for δ_{air}), measured values using a multispectrum fit (green), and a DPL fit using the measured value at each temperature (blue). Right: six of the 29 transmission measurements that were used to calculate the measurement values (D), the residual when comparing against a model using HITRAN parameters (E) and the MultiSpectrum Fit of This Work (MSF TW) with SPL TD parameters (F), respectively. Note the weak absorption at 1300 K increasing the uncertainty of the retrieved a_w value.

For both γ_{air} and δ_{air} , the SPL parameterization reasonably represents the TD of this transition for the temperature range measured in this work, a trend observed in almost all (over 96%) of the isolated transitions studied. As highlighted in Figure 4, panel A, HITRAN values for γ_{air}^0 and $n_{\gamma,air}$ generally match measurements of other isolated transitions in this analysis. Similarly, a_w (panel C) for this transition is nominally constant, as was assumed using the parameterization shown in Equation 1.

For the transitions where δ_{air}^0 and $n_{\delta,air}$ were calculated using the multispectrum fitting criteria described previously (77% of the 221 transitions), only a small fraction (~4%) of observed $\delta_{air}(T)$ trends were better represented with a fit using DPL TD across the measured temperature range. For these transitions where SPL TD was measured, the improvements compared to DPL TD in this temperature range were generally small. This does not imply that SPL and DPL parameterizations both adequately represent δ_{air} TD at all temperatures, only that the upper limit for multispectrum fit uncertainties ($\pm 0.005 \text{ cm}^{-1}$ and ± 0.13 , for δ_{air}^0 and $n_{\delta,air}$ respectively) successfully filtered out most transitions where SPL TD gave poor results. This contrasts with Part I for pure H_2O , where the low pressures (max pressure of 16 vs 600 Torr) complicated efforts to identify and reject transitions where SPL TD resulted in poor fits. Furthermore, the DPL parameterization appears to overfit the measured $\delta_{air}(T)$ datapoints in Figure 4, panel B, likely giving unreasonable extrapolations below 300 K, where the absorption would be the strongest for this transition.

Figure 5 shows γ_{air} , δ_{air} , and a_w calculated as a function of temperature for the $v_1 + v_3$ ($12_{1,11} \leftarrow 13_{1,12}$) transition, with the transmission data again shown on the right. For this high-J transition, both the HITRAN and multispectrum fit values for γ_{air}^0 at 300 K do not match the measured value shown in panel A. We note that for this type of high-J transition, the discrepancy has no discernable effect on the 300 K residual shown in panel F due to the weak absorption at lower temperature. The DPL parameterization provides the best fit for γ_{air} at 300 K. Both DPL and SPL TD provide reasonable predictions above 500 K where the strongest absorption is observed. A similar trend was observed in approximately 3% of the 221 isolated transitions analyzed.

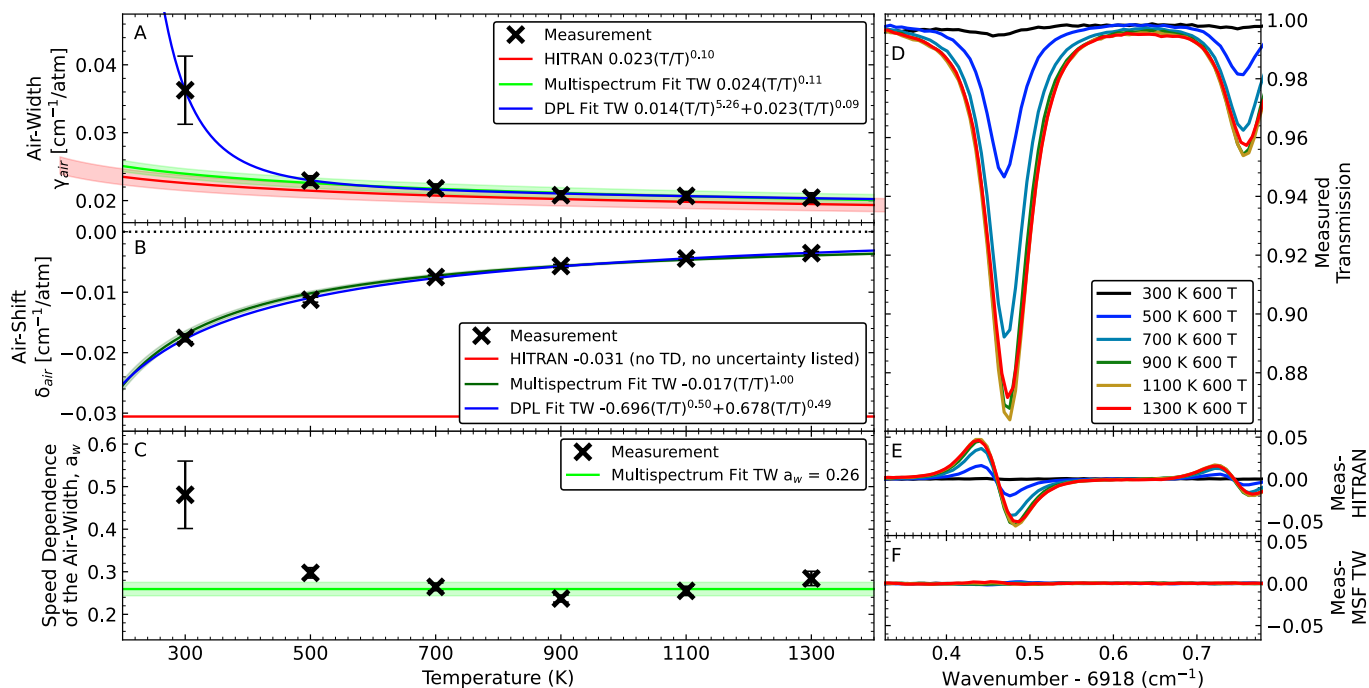


Figure 5: Left: γ_{self} (panel A), δ_{self} (B), and a_w (C) for the $v_1 + v_3$ ($12_{1,11} \leftarrow 13_{1,12}$) transition as a function of temperature. Measured values at each temperature are shown in black, with database values from HITRAN2020 (red, no TD), measured values using a multispectrum fit (green), and a DPL fit using the measured value at each temperature (blue). Right: six of the 29 transmission measurements that were used to calculate the measurement values (D), the residual when comparing against the HITRAN model ϵ and the MultiSpectrum Fit of This Work (MSF TW) with SPL TD parameters (F), respectively. Note the weak absorption at 300 K increasing the uncertainty of the retrieved a_w value.

The use of SPL TD for δ_{air} , with an updated value for δ_{air}^0 compared to HITRAN, improves the residual between measurement and model (panel E vs F). While more SD variation is observed for this transition, the majority of the $a_w(T)$ parameters, particularly those at conditions with sufficient SNR to impact the residual (i.e. above 500 K), match the nominal 0.26 measured value when using the multispectrum fit.

The two transitions shown exhibit behavior commonly observed in the other 221 isolated transitions that were strong enough to measure at all six temperatures: (1) when γ_{air} TD calculations benefited from fits using the DPL parameterization ($\sim 3\%$ of the transitions), SPL TD gave reasonable estimates of parameters at temperatures where the absorption was the strongest and (2) for both γ_{self} and δ_{self} , when SPL fit parameters gave similar results to DPL fit parameters within the measured temperature range ($\sim 96\%$ of transitions), the DPL parameterization was prone to overfitting, providing questionable extrapolations outside of the measured temperature range. These trends are entirely due to the limited quantity and range of temperatures inherent to physical measurements in a furnace without a cryostat, such as those presented in this work, and are in no way indicative of general DPL suitability for TD parameterization.

With a focus on generating a database optimized for ambient to high-temperature measurements, the authors view the SPL TD parameterization as an effective tool to extract information from absorption features with overlapping transitions, a common occurrence for H_2O in this region, such that a model generated using the database matches observed absorption. From this analysis we concluded that the SPL TD was able to achieve these aims – high fidelity within the measurement range, plausible predictions outside of the measurement range, and maximum improvement for overlapping transitions and transitions only visible at a subset of temperatures. For this reason, and because it would not be possible to fit DPL to most of the 3366 transitions measured, we focused our efforts on SPL parameterizations for both widths and shifts. A companion study will use this data to further explore DPL parameters for select, high-SNR transitions.

In addition to TD of γ_{air} and δ_{air} , the assumption that a_w was constant with respect to γ_{air} has the potential to impact the fidelity of retrievals. As shown in Figure 4 and Figure 5, a_w is found to be generally constant for the

transitions measured at these temperatures when parameterizing γ_{air} using the SPL. Among all 221 transitions, a_w varied by nominally $\pm 5.2\%$, slightly more than the $\pm 3.9\%$ observed for pure H₂O absorption.

As described by Lisak et al. in Equation 20 of [42] and Ghysels et al. in Equation 13 of [43], a_w for an absorbing gas in air is postulated to only be a function of $n_{\gamma,air}$, without a unique TD, as described by Equation 9:

$$a_w = \frac{2}{3}(1 - n_{\gamma,air}) \frac{\alpha}{1 + \alpha} \quad (9)$$

Where α is the mass ratio of the perturbing vs absorbing molecule. In exploring this relationship for H₂O in air, we recognize that the applicability of Equation 9 is inherently coupled to γ_{air} SPL TD through $n_{\gamma,air}$ and that air is a gas mixture predominantly composed of two molecules with slightly different mass. The goal of this analysis is to identify additional methods to extrapolate a_w beyond the transitions directly measured in this work. Similar to the studies described by Hartmann et al. [44], however, we did not observe this relationship for pure H₂O.

Results and Discussion

The transmission spectrum shown previously in Figure 3 is presented again in the top row of Figure 6 with the addition of residuals between the measurement and the HITRAN2020 database (HT, second row), the updated database in This Work (TW) using the VP (third row), and the database using the full SDVP (bottom row). As shown in Panel A, the SDVP database best matches the 1300 K measurement, followed by the updated VP database. Root Mean Square (RMS) residual error decreases from 0.0047 (HT) to 0.0010 (VP) and 0.007 (SDVP) between 6750-7501 cm⁻¹ for the condition shown (with average RMS for all measurements improving from 0.0025 to 0.0008 and 0.0006 for HT, VP, and SDVP, respectively).

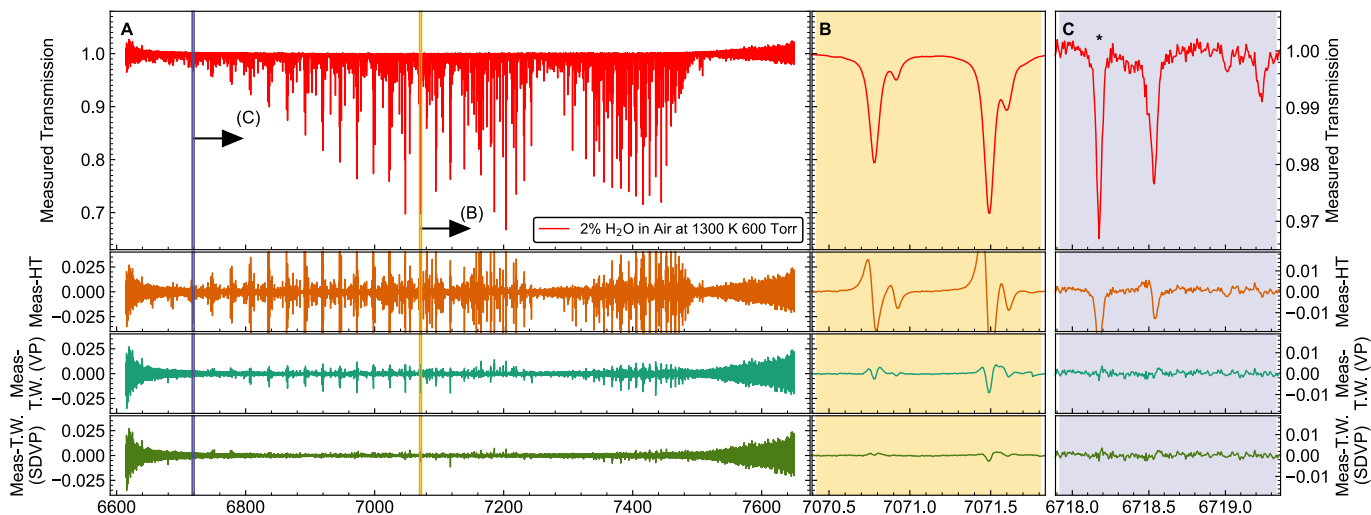


Figure 6: Normalized, measured transmission spectrum of 2% H₂O in air at 1300 K and 600 Torr over a 91.4 cm pathlength (top) with the original residual with respect to HITRAN2020 (HT, second row), the residual from the multispectrum fit employed in This Work (TW) and the VP (third row), and the SDVP (bottom). The entire measured bandwidth is shown in Panel A, with a representative region of strong absorption features shown in Panel B using the same y axis. Panel B highlights the improvement in spectral shifts in the updated database along with the importance of SD between the VP and SDVP. Weakly absorbing features, including a feature that was not included in the HITRAN2020 database (6718.2 cm⁻¹, marked with *), are shown in Panel C. Due to the limited SNR for these weak features, minimal difference is seen between the VP and SDVP parameterizations.

Zooming in on strong absorption features, in Panel B we see that the largest improvements to the database were spectral shifts, in particular at elevated temperatures. TD shift values are not presently available in HITRAN and, as described by Gamache and Vispoel [38] and Stolarczyk et al. [39], would likely be poorly described by the linear pressure shift TD model currently used in the HITRAN database format at these temperatures. The improvement of feature width between the VP and SDVP is highlighted in the bottom two panels. A small residual is still visible at

7071.5 cm^{-1} . After separating the measurements by temperature and evaluating shifts and widths for all measurements at a given temperature, we determined that this lingering residual is due to the difference in TD between the Lorentzian and SD width that is not captured when using a_w for SD.

We highlight the improvements by showing a sample of weakly absorbing transitions in Panel C of Figure 6. As described in Part I, the feature depicted at the left (6718.2 cm^{-1} , marked with *) is not presently included in the HITRAN database. Due to the reduced SNR of these weakly absorbing features, SD has minimal impact on the observable residual.

We summarize the quantity of updated parameters from this work, grouped by vibrational band catalogued in the HITRAN2020 database in Table 2. The complete line-by-line database is included in the supplementary material of this paper. In total, we updated at least some parameters for 3347 unique transitions, 99.4% of which originate from main isotopologue H_2^{16}O (99.7% at natural abundance). Throughout the subsequent sections, we share more detailed analysis and discussion for each of the parameters described in Table 2.

Table 2: Summary of the number of features analyzed for various vibrational bands and isotopologues of H_2O visible in this study. Uncatalogued features that were observed were assumed to be of the main isotopologue (H_2^{16}O). An iterative fitting routine was used in the column order shown, first fitting line center and strengths, followed by width parameters, and finally shift. When fit uncertainties surpassed certainty limits, that value was not updated. An additional 62 features not included in these totals were determined to have line strengths lower than those listed in HITRAN2020. 40 uncatalogued features were also identified with line strengths too weak to be reliably retrieved.

Vibrational Band	Max J''	Air- Width	Temperature- Dependence of the Air-Width	Speed- Dependence of the Air-Width	Air-Shift	Temperature- Dependence of the Air-Shift
H_2^{16}O						
101 \leftarrow 000	22	880	524	446	404	254
200 \leftarrow 000	20	627	336	249	223	140
021 \leftarrow 000	20	463	271	214	157	87
111 \leftarrow 010	19	394	88	62	59	22
031 \leftarrow 010	18	218	39	21	1	0
002 \leftarrow 000	20	184	31	18	9	6
120 \leftarrow 000	19	125	34	10	3	0
201 \leftarrow 100	12	93	0	0	0	0
210 \leftarrow 010	17	90	3	2	0	0
121 \leftarrow 020	14	66	0	0	0	0
041 \leftarrow 020	13	47	0	0	0	0
300 \leftarrow 100	11	47	2	0	0	0
102 \leftarrow 001	11	32	0	0	0	0
Other Bands	20	37	3	2	2	0
Uncatalogued		44	0	0	0	0
Subtotal		3347	1331	1024	858	509
H_2^{18}O						
101 \leftarrow 000	17	19	0	0	0	0
Total		3366	1331	1024	858	509

Air-Broadened Half-Width

Fit results for the 3322 air-broadened half-widths, γ_{air}^0 , measured in this work are shown in panel A of Figure 7 as a function of J'' with coloration based on the lower state energy, E'' . A slight offset of 0.9 Kc''/J'' is added to the x-axis to highlight the change of γ_{air}^0 through the oblate ($\text{Kc}'' = 0$) to prolate ($\text{Kc}'' = J''$) progression. Transitions not catalogued in HITRAN that were identified in Part I of this work are not included on this plot due to the lack of quantum assignments but are included in the supplemental material. HITRAN values for the corresponding transitions are shown in panel B, with the change between this work and HITRAN in panel C. In panels A and C we include measurement uncertainties from measurements in this work, as discussed at the end of this section. HITRAN uncertainties are shown in panel B, with arrows used to indicate unbounded values corresponding to transitions assigned uncertainty codes 3 (over 20%) and 2 (average or constant value). Insets in panels A and B highlight the variation in γ_{air}^0 as a function of Kc'' for $J'' = 9$.

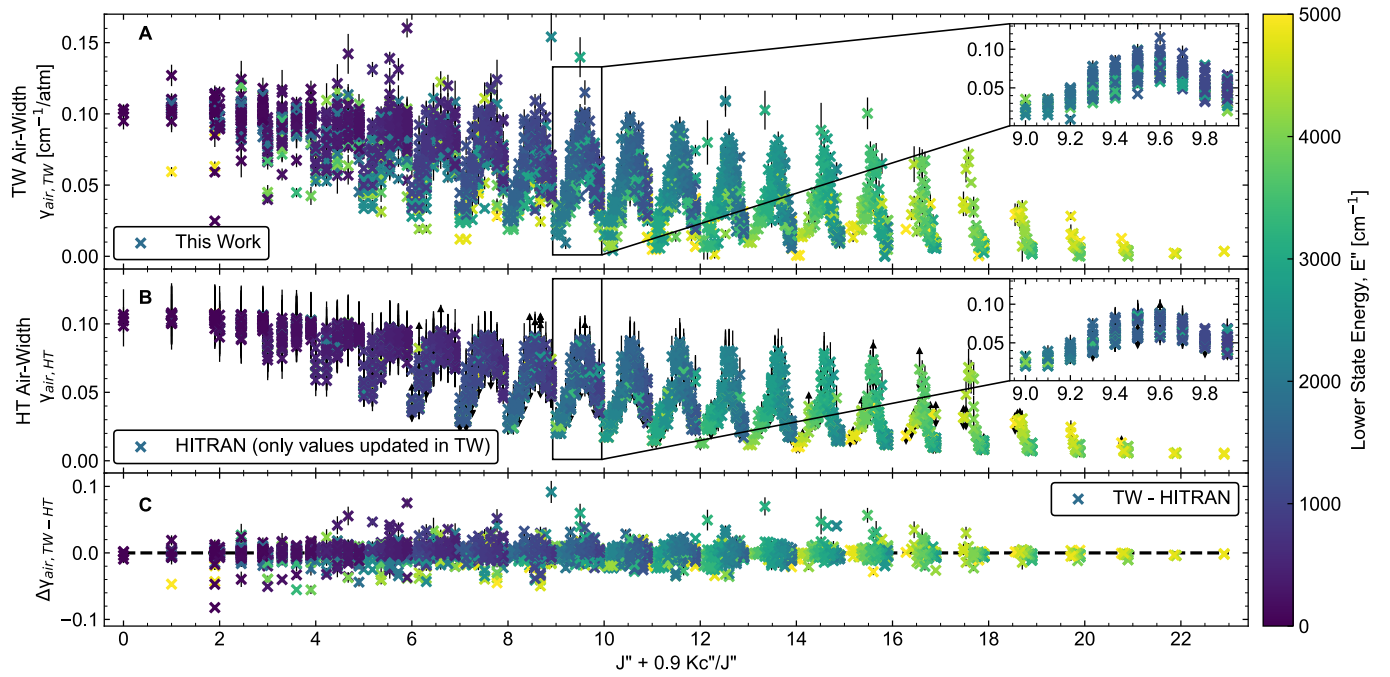


Figure 7: Measured (panel A) and HITRAN (panel B) air-broadened width values, γ_{air}^0 , as a function of rotational quantum number J'' with a small Kc''/J'' offset. Insets in the upper right highlight the variation of γ_{air}^0 as a function of Kc'' at $J'' = 9$. Panel C shows the difference in γ_{air} between this work and HITRAN.

In aggregate, we see scattered, though unbiased, agreement between this work and HITRAN, with a linear correlation between the two of $\gamma_{air,TW}^0 = -0.0016 + 1.01\gamma_{air,HT}^0$ ($R^2 = 0.88$, not shown in Figure 7). The HITRAN values for the majority of updated features (69%) originate from approximations of semi-empirical coefficients from section 4.2.2 in Jacquemart et al. [14], [45] with an additional 22% of HITRAN values derived by Gamache using the Complex Robert Bonamy formulation [46] (see γ_{air}^0 ref. 60 in [14]). We observe the best agreement between this work and the measurements of Toth [47], [48] (8% of the updated transitions), with $-6 \pm 7\%$ difference when comparing against $\gamma_{air,SDVP}^0$. The offset with respect to Toth's measurements is reduced when comparing against our retrievals using only the Voigt profile, $\gamma_{air,VP}^0$, with a mean difference of $-2 \pm 8\%$. On average, our retrieval for $\gamma_{air,VP}^0$ (not shown) was 3% smaller than $\gamma_{air,SDVP}^0$ for the same transitions. Note that the HITRAN database does not include SD effects on spectral widths. These relationships highlight the importance of both semi-empirical calculations to compute large quantities of spectral parameters with general accuracy and reference measurements of individual transitions for high-fidelity retrievals.

Total uncertainty for each transition in this work was estimated using the method of Cole et al. [23], which is to sum the uncertainties in quadrature, including statistical (averaging ± 0.003 or $\pm 4.5\%$), pressure ($\pm 0.26\%$), concentration ($\pm 2.9\%$), and temperature (per Ref. [49]) uncertainties.

Temperature-Dependence (TD) of the Air-Width

In Figure 8 we show the single power law TD of the 1331 air-width values we measured in this work, $n_{\gamma,air}$, using the same adjusted J'' x-axis as Figure 7. Comparable to Figure 7, panels A, B, and C show $n_{\gamma,air,TW}$ measured in this work, $n_{\gamma,air,HT}$ in the HITRAN database, and the difference between $n_{\gamma,air,TW}$ and $n_{\gamma,air,HT}$, respectively. Over 98% of the HITRAN features updated in this work are assigned HITRAN uncertainty code 2, indicating that $n_{\gamma,air,HT}$ is an average or estimate, as opposed to being assigned a bounded uncertainty (i.e. less than 10%). In spite of this, we observe similar structure between this work and HITRAN, as shown in the insets for both values of $n_{\gamma,air}$. The majority of transitions with $J'' > 15$ are strongly absorbing doublets where $n_{\gamma,air}$ could be influenced by small errors in center frequency spacing between the line pair or by line mixing. Line-mixing effects are not explored in this

study due to the congested nature of H₂O absorption in this region and the large number of transitions measured. We note that seven high- J'' outlier values of $\Delta n_{\gamma,air,TW-HT}$ in panel C were cropped from the image to better highlight the change of the other 1326 transitions ($J'' = 12, 12, 15, 17, 17, 18, 18$). These transitions are included in panel A and the supplemental materials. All but one are indistinguishably overlapping doublet pairs.

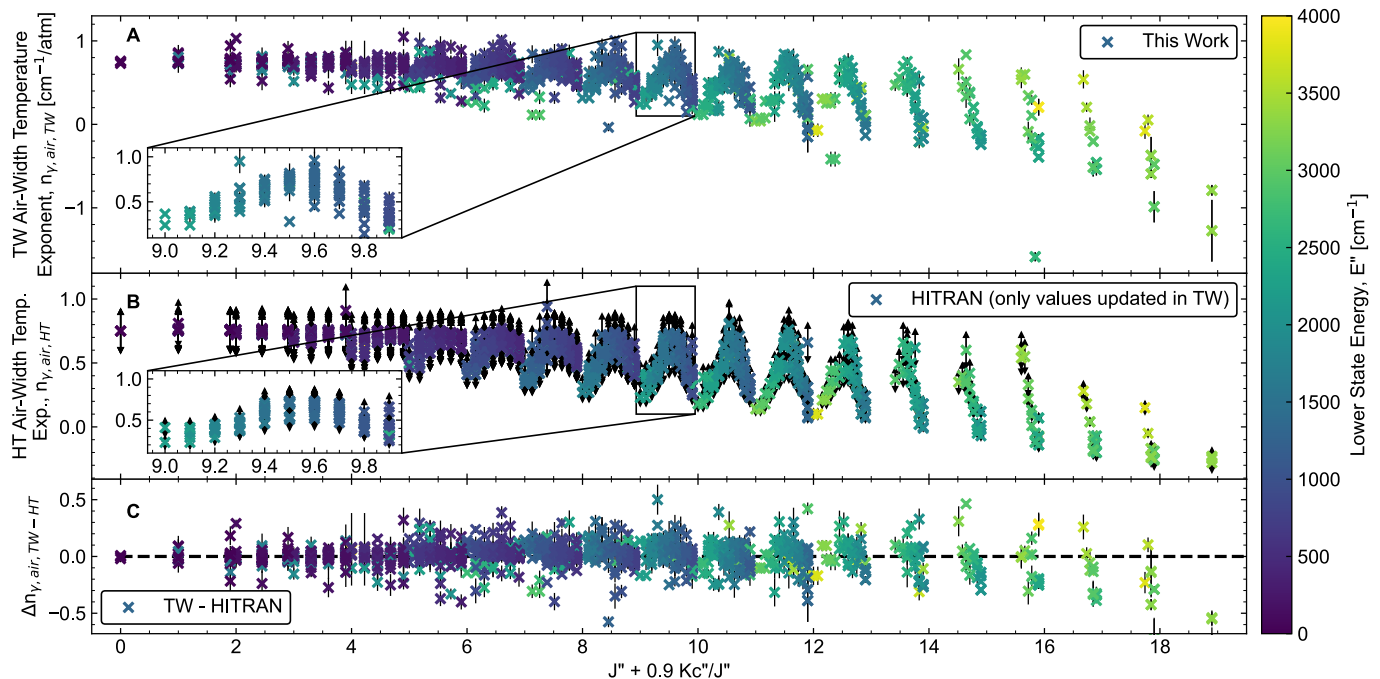


Figure 8: Measured (panel A) and HITRAN (panel B) TD of the air-broadened width values, $n_{\gamma,air}$, as a function of rotational quantum number J'' with a small Kc''/J'' offset. Insets in panels A and B highlight the variation of $n_{\gamma,air}$ as a function of Kc'' at $J'' = 9$. Panel C shows the difference in $n_{\gamma,air}$ between this work and HITRAN.

We observe general agreement between $n_{\gamma,air}$ from this work and HITRAN, as shown in Figure 6. For values where $n_{\gamma,air,HT}$ was larger than zero, $n_{\gamma,air,TW} = -0.0255 + 1.06n_{\gamma,air,HT}$ with a R^2 correlation of 0.79. For all 1331 values, $n_{\gamma,air,TW}$ was, on average, 9% larger than $n_{\gamma,air,HT}$. Noting that $n_{\gamma,air,HT}$ does not include SD, we observed that $n_{\gamma,air,HT}$ is, on average, only 2% larger than $n_{\gamma,air,TW,VP}$ (not shown).

Due to the correlation between $n_{\gamma,air}$ and γ_{air}^0 parameters, it is not possible to know $n_{\gamma,air}$ better than the foundational parameter γ_{air}^0 , as discussed by [23], [35], [50], [51]. As such, the total uncertainty for $n_{\gamma,air}$ was estimated by adding the relative $n_{\gamma,air}$ statistical uncertainty in quadrature with the relative γ_{air}^0 uncertainty multiplied by $\sqrt{2} \ln(T_{max}/T_{min})^{-1}$, per [23], [50], [51] and as implemented in Part I [13].

Finally, in Figure 9 we compare measured values for $n_{\gamma,air}$ and γ_{air}^0 from this work. We observe a linear relationship, as shown on the plot, down to approximately γ_{air}^0 of 0.02. Comparable to Part I for H₂O self-widths, $n_{\gamma,air}$ rapidly decreases near γ_{air}^0 of zero for high-temperature transitions. These transitions are frequently not visible at lower temperatures, such as 300 K, making the ambient temperature reference γ_{air}^0 an extrapolation that is heavily dependent on the TD parameterization, in this case a single power law $n_{\gamma,air}$. At elevated temperatures, the Doppler width also becomes the dominant contributor to the total width, further obscuring retrievals of γ_{air}^0 and $n_{\gamma,air}$. Similar to Figure 8, four transitions where $n_{\gamma,air} < -0.6$ are not shown in Figure 9 to best highlight global trends. These transitions can be found in the supplemental database provided with this work.

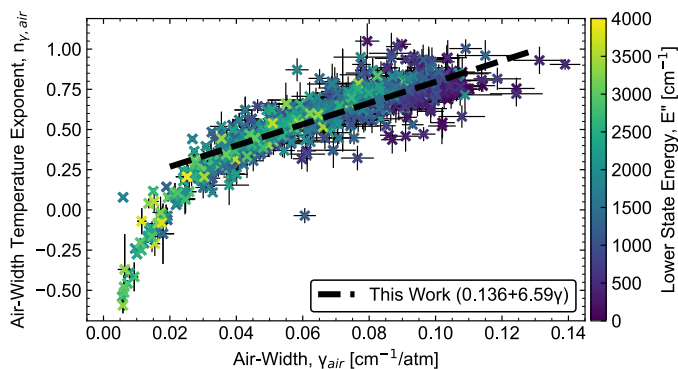


Figure 9: TD of the air-width, $n_{\gamma,air}$, as a function of the air-width, γ_{air}^0 , for all transitions updated in this work. We calculated a trend line between the parameters (for $\gamma_{air}^0 > 0.02$) and found a correlation of $R^2 = 0.74$ with the fit parameters shown in the legend.

Speed-Dependence (SD) of the Air-Width

SD of the air-width, a_w , for the 1024 transitions where this parameter could be retrieved, is shown in Figure 10 as a function of J'' . Unlike self-width a_w values, which were generally constant, a_w with air as the collisional partner exhibit a positive correlation with J'' , as shown by the line of best fit with a slope of $0.011J''$ ($R^2 = 0.3$). While a_w is plotted with a slight Kc'' offset, we were not able to identify any sub-structure correlated with Kc'' in the a_w parameters, comparable to the insets shown in Figure 7 and Figure 8 for γ_{air}^0 and $n_{\gamma,air}$, respectively. We calculated a_w values using Equation 9 with an average value of α to represent the average mass of air. We observed similar average values (0.19 ± 0.08 and 0.18 ± 0.11 when retrieved and calculated, respectively). The calculated and the retrieved values show moderate agreement up to approximately J'' of 14 when averaging all $n_{\gamma,air}$ values at a given J'' . Taken individually, calculated values of a_w have a negative R^2 value (worse agreement than the mean) with respect to their measured counterparts. While slightly better at predicting a_w for air-H₂O collisions than pure-H₂O, our result taken along with other studies [22], [36], [52], [53], [54] identified by Hartmann et al. [44], further supports the hypothesis of Wilzewski et al. that the temperature range, molecule, perturbing molecule, or transition measured impacts the applicability of Equation 9 [54].

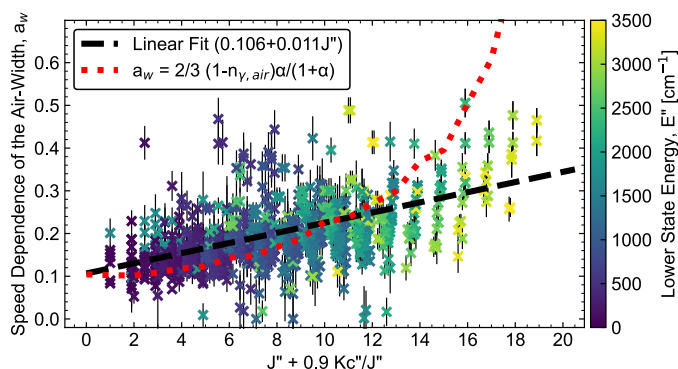


Figure 10: SD of the air-width, a_w , as a function of J'' with an offset of Kc'' . A linear best fit to the data is shown in black ($R^2 = 0.3$) to highlight the upward trend in the data. Additionally, measured values of $n_{\gamma,air}$ and Equation 9 were used to calculate a_w , with the red line showing the average results for each J'' [43].

Like Part I [13], TD of the SD was not included as a unique retrieved parameter in this study. Instead we assume that a_w , the ratio of SD and the Lorentz width, is constant with temperature. We calculated a_w at each temperature for 221 strong and isolated features, and observed variations of $\pm 5.2\%$, which is slightly larger than the 3.9% observed in Part I [13]. Total uncertainties for a_w were calculated with the same technique used for γ_{air}^0 with an additional $\pm 5.2\%$ included for the lack of TD. For reference, the average statistical uncertainty is ± 0.018 .

Air Pressure Shift

In Figure 11 we show the 858 air pressure shift, δ_{air}^0 , values we retrieved in this work using the same adjusted J'' x-axis as shown previously. The strong trends with respect to Kc'' observed for $n_{\gamma,air}$ and γ_{air}^0 are not as visible for δ_{air}^0 . Panels A, B, and C show δ_{air}^0 measured in this work, δ_{air}^0 in the HITRAN database, and the difference between $\delta_{air,TW}^0$ and $\delta_{air,HT}^0$, respectively.

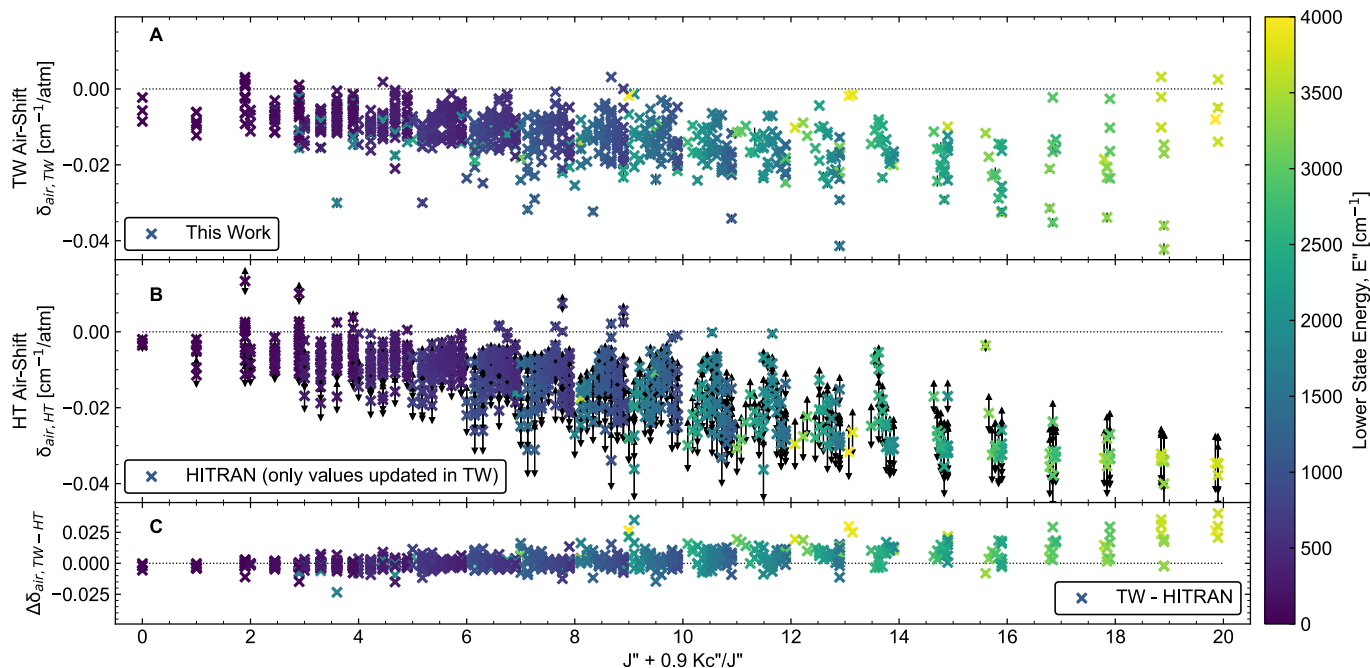


Figure 11: Measured (panel A) and HITRAN (panel B) air-shift, δ_{air}^0 , as a function of rotational quantum number J'' with a small Kc''/J'' offset. Panel C shows the difference in δ_{air}^0 between this work and HITRAN.

From Figure 11, we note the bias between $\delta_{air,TW}^0$ and $\delta_{air,HT}^0$ beginning near $J'' = 12$ and clearly visible in panel C, where $\delta_{air,HT}^0$ is consistently more negative than $\delta_{air,TW}^0$. The majority of HITRAN δ_{air}^0 values updated in this work originate from potential energy surface calculations for H_2O-N_2 collisions performed by Vispoel et al. in [55] (63% of features) and [56] (22%) that were combined with oxygen data from Gamache and Vispoel for use in the HITRAN database [14]. For δ_{air}^0 taken from these sources, RMS errors relative to this work were 0.008 and 0.005 cm^{-1} for [55] and [56], respectively. In contrast, 14% of the δ_{air}^0 values were taken from a dedicated study of room temperature H_2O and air presented by Toth [48]. The RMS error for these transitions was only 0.001 cm^{-1} . Of the 121 Toth transitions updated in this work, only six have double digit J'' (maximum J'' of 12) because Toth only measured absorption at room temperature. All but one of the HITRAN values for δ_{air}^0 at $J'' > 12$, parameters with the observed bias relative to this work shown in panel C, originate from the potential energy surface calculations of [55] and [56]. The existence of δ_{air}^0 values for these transitions highlights the importance of ab initio calculations for determining parameters that have not been measured, even if those calculations have larger errors than direct measurements. We hope the measurements presented in this work can be used in partnership with future potential energy surface calculations to better predict δ_{air}^0 , especially for high- J'' H_2O transitions.

Total uncertainty values for δ_{air}^0 were calculated using the same technique as Part I [13], noting that the measured pressure range for H_2O in air is considerably larger than pure H_2O vapor (600 vs 16 Torr). When calculating total uncertainty, we used the same terms identified previously for γ_{air} with an additional wavenumber uncertainty term estimated as the DCS wavenumber uncertainty divided by $P_{max}\delta_{air}^0$, the maximum observed shift under the conditions measured (600 Torr or 0.79 atm).

Temperature-Dependence (TD) of the Air-Shift

Figure 12 shows the 509 retrieved single power law TD of the air-shift values, $n_{\delta,air}$, plotted as a function of J'' with a Kc'' offset and coloration based on lower state energy comparable to previous figures. In contrast to $n_{\gamma,air}$, we observe $n_{\delta,air}$ increasing as a function of J'' . Based on the single power law parameterization, a larger $n_{\delta,air}$ at high J'' would more aggressively attenuate the larger magnitude of δ_{air}^0 for these high-temperature transitions, reducing the observed shift.

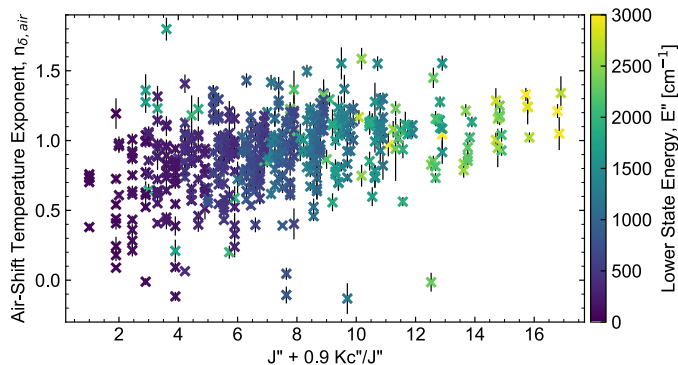


Figure 12: Measured TD of the air-shift, $n_{\delta,air}$, as a function of J'' with a $0.9 Kc''/J''$ offset, colored based on the vibrational assignment of each transition.

In Figure 13 we plot $n_{\delta,air}$ and δ_{air}^0 for the 509 transitions where both were measured, comparable to the inter-comparison of $n_{\gamma,air}$ and γ_{air}^0 shown previously in Figure 9. Like Figure 9, both $n_{\gamma,air}$ and $n_{\delta,air}$ trend downward to zero or below when γ_{air} and δ_{air}^0 approach zero, highlighting the correlation between TD and the reference value.

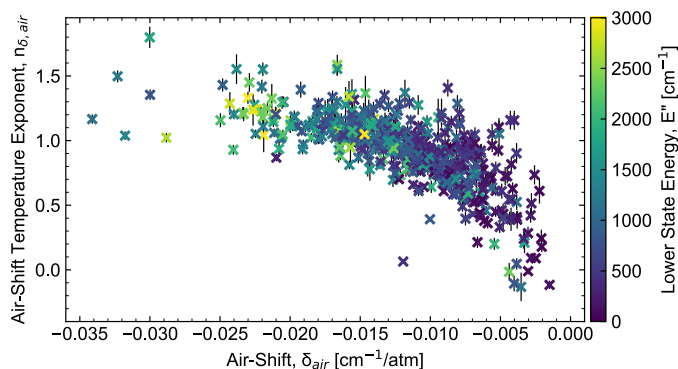


Figure 13: TD of the air-shift, $n_{\delta,air}$, as a function of the air-shift, δ_{air}^0 , for all transitions updated in this work.

Total uncertainty was calculated by combining the statistical uncertainty for $n_{\delta,air}$ and that of δ_{air}^0 using the same method of relating uncertainty in γ_{air}^0 and $n_{\gamma,air}$ shared previously. Using the standalone δ_{air}^0 without incorporating $n_{\delta,air}$ should be done with caution given the interrelated nature of δ_{air}^0 and $n_{\delta,air}$.

Conclusions

We present 7088 air-broadening parameters for 3366 unique absorption transitions of H_2O between $6600-7650 \text{ cm}^{-1}$. These parameters include significant updates to the temperature dependence of the air-shift that are difficult to measure at ambient γ temperatures and thus have not been broadly catalogued using traditional spectroscopic techniques.

We determine the new line shape parameters using 29 DCS H_2O absorption spectra between 300 and 1300 K and 20 to 600 Torr air, with an average residual noise of $8.0E-4$ (absorbance units) and $\pm 1.7E-4 \text{ cm}^{-1}$ wavenumber

uncertainty. With these measurements, updates are made to transitions with line strengths as low as $3\text{E-}31\text{ cm}^{-1} / (\text{molecule cm}^{-2})$.

Building on the database presented in Part I, we experimentally determine 3366 γ_{air}^0 , 1331 $n_{\gamma,air}$, and 1000 a_w parameters. We observe good agreement between γ_{air}^0 and $n_{\gamma,air}$ values measured in this work compared to those in the HITRAN database, which predominantly originate from semi-empirical calculations [14], [45]. We hope these new values for γ_{air}^0 and $n_{\gamma,air}$ can be used to improve these semi-empirical calculations, especially for high-temperature transitions.

We present 858 updated values for δ_{air}^0 and 509 newly added values for $n_{\delta,air}$. Updated δ_{air}^0 values were shown to agree well with both semi-empirical and experimentally determined HITRAN values up to J'' of 14, beyond which a bias is observed in HITRAN values. The inclusion of $n_{\delta,air}$ visibly improved spectral residuals of high-temperature measurements.

In addition to the SDVP values presented, values using the Voigt profile were also retrieved for situations where the fidelity of SD narrowing is not required (e.g. low SNR measurements). Overall, compared to the HITRAN2020 database, spectral residuals across all measured conditions were reduced by a factor of 4.2 in this work using SDVP parameters, improving our understanding of H₂O absorption in air, especially at combustion relevant conditions.

Declaration of Competing Interests

The authors declare that they have no known competing financial interests or personal relationships that could have appeared to influence the work reported in this paper.

Acknowledgements

This work was funded through NASA's Exoplanetary Research Program (80NSSC18K0351), the Air Force Research Laboratory (AFRL) (FA8650-20-2-2418), and Air Force Office of Scientific Research (AFOSR) (FA9550-20-1-0328). Portions of this research were performed at the Jet Propulsion Laboratory, California Institute of Technology, under contract with the National Aeronautics and Space Administration and California Institute of Technology. Government sponsorship acknowledged.

Works Cited

- [1] D. D. B. Koll and T. W. Cronin, "Earth's outgoing longwave radiation linear due to H₂O greenhouse effect," *Proc. Natl. Acad. Sci. U.S.A.*, vol. 115, no. 41, pp. 10293–10298, Oct. 2018, doi: 10.1073/pnas.1809868115.
- [2] I. M. Held and B. J. Soden, "Water Vapor Feedback and Global Warming," *Annu. Rev. Energy. Environ.*, vol. 25, no. 1, pp. 441–475, Nov. 2000, doi: 10.1146/annurev.energy.25.1.441.
- [3] M. R. Swain *et al.*, "Water, Methane, and Carbon Dioxide Present in the Dayside Spectrum of the Exoplanet HD 209458b," *The Astrophysical Journal*, vol. 704, no. 2, 2009, doi: 10.1088/0004-637X/704/2/1616.
- [4] G. Tinetti, J. Tennyson, C. A. Griffith, and I. Waldmann, "Water in exoplanets," *Philosophical Transactions of the Royal Society A*, vol. 370, 2012, doi: 10.1098/rsta.2011.0338.
- [5] D. Yun *et al.*, "Spatially resolved mass flux measurements with dual-comb spectroscopy," *Optica*, vol. 9, no. 9, p. 1050, Sep. 2022, doi: 10.1364/OPTICA.459009.
- [6] C. S. Goldenstein, C. A. Almodóvar, J. B. Jeffries, R. K. Hanson, and C. M. Brophy, "High-bandwidth scanned-wavelength-modulation spectroscopy sensors for temperature and H₂O in a rotating detonation engine," *Meas. Sci. Technol.*, vol. 25, no. 10, p. 105104, Oct. 2014, doi: 10.1088/0957-0233/25/10/105104.
- [7] J. T. C. Liu *et al.*, "Near-infrared diode laser absorption diagnostic for temperature and water vapor in a scramjet combustor," *Appl. Opt.*, vol. 44, no. 31, p. 6701, Nov. 2005, doi: 10.1364/AO.44.006701.
- [8] Z. Qu, R. Ghorbani, D. Valiev, and F. M. Schmidt, "Calibration-free scanned wavelength modulation spectroscopy – application to H₂O and temperature sensing in flames," *Opt. Express*, vol. 23, no. 12, p. 16492, Jun. 2015, doi: 10.1364/OE.23.016492.

- [9] O. Witzel, A. Klein, S. Wagner, C. Meffert, C. Schulz, and V. Ebert, "High-speed tunable diode laser absorption spectroscopy for sampling-free in-cylinder water vapor concentration measurements in an optical IC engine," *Appl. Phys. B*, vol. 109, no. 3, pp. 521–532, Nov. 2012, doi: 10.1007/s00340-012-5225-0.
- [10] O. Witzel *et al.*, "VCSEL-based, high-speed, in situ TDLAS for in-cylinder water vapor measurements in IC engines," *Opt. Express*, vol. 21, no. 17, p. 19951, Aug. 2013, doi: 10.1364/OE.21.019951.
- [11] S. Wehe, D. Baer, and R. Hanson, "Tunable diode-laser absorption measurements of temperature, velocity, and H₂O in hypervelocity flows," in *33rd Joint Propulsion Conference and Exhibit*, Seattle, WA, USA: American Institute of Aeronautics and Astronautics, Jul. 1997. doi: 10.2514/6.1997-3267.
- [12] J. Girard *et al.*, "Characterization of the T₅ Reflected Shock Tunnel Freestream Temperature, Velocity, and Composition using Laser Absorption Spectroscopy," in *AIAA Propulsion and Energy 2021 Forum*, VIRTUAL EVENT: American Institute of Aeronautics and Astronautics, Aug. 2021. doi: 10.2514/6.2021-3525.
- [13] S. C. Egbert, K. Sung, S. C. Coburn, B. J. Drouin, and G. B. Rieker, "Water-Vapor Absorption Database using Dual Comb Spectroscopy from 300–1300 K Part I: Pure H₂O, 6600 to 7650 cm⁻¹," *Journal of Quantitative Spectroscopy and Radiative Transfer*, Feb. 2024, doi: 10.1016/j.jqsrt.2024.108940.
- [14] I. E. Gordon *et al.*, "The HITRAN2020 molecular spectroscopic database," *Journal of Quantitative Spectroscopy and Radiative Transfer*, vol. 277, p. 107949, Jan. 2022, doi: 10.1016/j.jqsrt.2021.107949.
- [15] L. S. Rothman *et al.*, "HITEMP, the high-temperature molecular spectroscopic database," *Journal of Quantitative Spectroscopy and Radiative Transfer*, vol. 111, no. 15, pp. 2139–2150, Oct. 2010, doi: 10.1016/j.jqsrt.2010.05.001.
- [16] O. L. Polyansky, A. A. Kyuberis, N. F. Zobov, J. Tennyson, S. N. Yurchenko, and L. Lodi, "ExoMol molecular line lists XXX: a complete high-accuracy line list for water," *Monthly Notices of the Royal Astronomical Society*, vol. 480, no. 2, pp. 2597–2608, Oct. 2018, doi: 10.1093/mnras/sty1877.
- [17] T. Delahaye *et al.*, "The 2020 edition of the GEISA spectroscopic database," *Journal of Molecular Spectroscopy*, vol. 380, p. 111510, Jul. 2021, doi: 10.1016/j.jms.2021.111510.
- [18] M. A. Koshelev *et al.*, "Water vapor line profile at 183-GHz: Temperature dependence of broadening, shifting, and speed-dependent shape parameters," *Journal of Quantitative Spectroscopy and Radiative Transfer*, vol. 262, p. 107472, Mar. 2021, doi: 10.1016/j.jqsrt.2020.107472.
- [19] N. H. Ngo *et al.*, "Intensities and shapes of H₂O lines in the near-infrared by tunable diode laser spectroscopy," *Journal of Quantitative Spectroscopy and Radiative Transfer*, vol. 113, no. 11, pp. 870–877, Jul. 2012, doi: 10.1016/j.jqsrt.2011.12.007.
- [20] N. H. Ngo, D. Lisak, H. Tran, and J.-M. Hartmann, "An isolated line-shape model to go beyond the Voigt profile in spectroscopic databases and radiative transfer codes," *Journal of Quantitative Spectroscopy and Radiative Transfer*, vol. 129, pp. 89–100, Nov. 2013, doi: 10.1016/j.jqsrt.2013.05.034.
- [21] P. J. Schroeder *et al.*, "Broadband, high-resolution investigation of advanced absorption line shapes at high temperature," *Phys. Rev. A*, vol. 96, no. 2, p. 022514, Aug. 2017, doi: 10.1103/PhysRevA.96.022514.
- [22] C. S. Goldenstein and R. K. Hanson, "Diode-laser measurements of linewidth and temperature-dependent lineshape parameters for H₂O transitions near 1.4 μm using Voigt, Rautian, Galatry, and speed-dependent Voigt profiles," *Journal of Quantitative Spectroscopy and Radiative Transfer*, vol. 152, pp. 127–139, Feb. 2015, doi: 10.1016/j.jqsrt.2014.11.008.
- [23] R. K. Cole, N. Hoghooghi, B. J. Drouin, and G. B. Rieker, "High-temperature absorption line shape parameters for CO₂ in the 6800–7000 cm⁻¹ region from dual frequency comb measurements up to 1000 K," *Journal of Quantitative Spectroscopy and Radiative Transfer*, vol. 276, p. 107912, Dec. 2021, doi: 10.1016/j.jqsrt.2021.107912.
- [24] N. A. Malarich *et al.*, "Dual frequency comb absorption spectroscopy of CH₄ up to 1000 Kelvin from 6770 to 7570 cm⁻¹," *Journal of Quantitative Spectroscopy and Radiative Transfer*, vol. 272, p. 107812, Sep. 2021, doi: 10.1016/j.jqsrt.2021.107812.
- [25] J.-D. Deschênes, P. Giaccarri, and J. Genest, "Optical referencing technique with CW lasers as intermediate oscillators for continuous full delay range frequency comb interferometry," *Opt. Express*, vol. 18, no. 22, p. 23358, Oct. 2010, doi: 10.1364/OE.18.023358.
- [26] J. Roy, J.-D. Deschenes, S. Potvin, and J. Genest, "Continuous real-time correction and averaging for frequency comb interferometry," *Nat Commun*, vol. 5, no. 1, p. 3375, May 2014, doi: 10.1038/ncomms4375.
- [27] I. Coddington, W. Swann, and N. Newbury, "Coherent dual-comb spectroscopy at high signal-to-noise ratio," *Phys. Rev. A*, vol. 82, no. 4, p. 043817, Oct. 2010, doi: 10.1103/PhysRevA.82.043817.

- [28] G.-W. Truong *et al.*, “Accurate frequency referencing for fieldable dual-comb spectroscopy,” *Opt. Express*, vol. 24, no. 26, p. 30495, Dec. 2016, doi: 10.1364/OE.24.030495.
- [29] I. Coddington, N. Newbury, and W. Swann, “Dual-comb spectroscopy,” *Optica*, vol. 3, no. 4, p. 414, Apr. 2016, doi: 10.1364/OPTICA.3.000414.
- [30] G.-W. Truong, K. C. Cossel, E. M. Waxman, F. R. Giorgetta, I. Coddington, and N. R. Newbury, “Phase Noise-Induced Biases in Coherent Dual-Comb Spectroscopy,” in *Conference on Lasers and Electro-Optics*, San Jose, California: OSA, 2016, p. SW1H.2. doi: 10.1364/CLEO_SI.2016.SW1H.2.
- [31] P. Guay, A. Tourigny-Plante, V. Michaud-Belleau, N. Bourbeau Hébert, A. Gouin, and J. Genest, “Understanding photodetection nonlinearity in dual-comb interferometry,” *OSA Continuum*, vol. 4, no. 9, p. 2460, Sep. 2021, doi: 10.1364/OSAC.435015.
- [32] J. Genest, M. Walsh, I. Coddington, N. Malarich, and K. Cossel, “Chasing systematic errors in dual comb spectroscopy,” *CLEO 2024 Application & Technology Topical Reviews*.
- [33] N. A. Malarich *et al.*, “Validation of open-path dual-comb spectroscopy against an O₂ background,” *Opt. Express*, vol. 31, no. 3, p. 5042, Jan. 2023, doi: 10.1364/OE.480301.
- [34] D. C. Benner, C. P. Rinsland, V. M. Devi, M. A. H. Smith, and D. Atkins, “A multispectrum nonlinear least squares fitting technique,” *Journal of Quantitative Spectroscopy and Radiative Transfer*, vol. 53, no. 6, pp. 705–721, Jun. 1995, doi: 10.1016/0022-4073(95)00015-D.
- [35] B. J. Drouin *et al.*, “Multispectrum analysis of the oxygen A-band,” *Journal of Quantitative Spectroscopy and Radiative Transfer*, vol. 186, pp. 118–138, Jan. 2017, doi: 10.1016/j.jqsrt.2016.03.037.
- [36] P. J. Schroeder *et al.*, “Speed-dependent Voigt lineshape parameter database from dual frequency comb measurements up to 1305 K. Part I: Pure H₂O absorption, 6801-7188 cm⁻¹,” *Journal of Quantitative Spectroscopy and Radiative Transfer*, vol. 210, pp. 240–250, May 2018, doi: 10.1016/j.jqsrt.2018.02.025.
- [37] J. Yang *et al.*, “Speed-dependent Voigt lineshape parameter database from dual frequency comb measurements at temperatures up to 1305 K. Part II: Argon-broadened H₂O absorption, 6801-7188 cm⁻¹,” *Journal of Quantitative Spectroscopy and Radiative Transfer*, vol. 217, pp. 189–212, Sep. 2018, doi: 10.1016/j.jqsrt.2018.05.040.
- [38] R. R. Gamache and B. Vispoel, “On the temperature dependence of half-widths and line shifts for molecular transitions in the microwave and infrared regions,” *Journal of Quantitative Spectroscopy and Radiative Transfer*, vol. 217, pp. 440–452, Sep. 2018, doi: 10.1016/j.jqsrt.2018.05.019.
- [39] N. Stolarczyk *et al.*, “Evaluation of different parameterizations of temperature dependences of the line-shape parameters based on ab initio calculations: Case study for the HITRAN database,” *Journal of Quantitative Spectroscopy and Radiative Transfer*, vol. 240, p. 106676, Jan. 2020, doi: 10.1016/j.jqsrt.2019.106676.
- [40] R. A. Toth, L. R. Brown, and C. Plymate, “Self-broadened widths and frequency shifts of water vapor lines between 590 and 2400 cm⁻¹,” *Journal of Quantitative Spectroscopy and Radiative Transfer*, vol. 59, no. 6, pp. 529–562, Jun. 1998, doi: 10.1016/S0022-4073(97)00144-1.
- [41] L. R. Brown, C. M. Humphrey, and R. R. Gamache, “CO₂-broadened water in the pure rotation and ν₂ fundamental regions,” *Journal of Molecular Spectroscopy*, vol. 246, no. 1, pp. 1–21, Nov. 2007, doi: 10.1016/j.jms.2007.07.010.
- [42] D. Lisak, A. Cygan, P. Wcisło, and R. Ciuryło, “Quadratic speed dependence of collisional broadening and shifting for atmospheric applications,” *Journal of Quantitative Spectroscopy and Radiative Transfer*, vol. 151, pp. 43–48, Jan. 2015, doi: 10.1016/j.jqsrt.2014.08.016.
- [43] M. Ghysels, Q. Liu, A. J. Fleisher, and J. T. Hodges, “A variable-temperature cavity ring-down spectrometer with application to line shape analysis of CO₂ spectra in the 1600 nm region,” *Appl. Phys. B*, vol. 123, no. 4, p. 124, Apr. 2017, doi: 10.1007/s00340-017-6686-y.
- [44] J.-M. Hartmann *et al.*, “Recent advances in collisional effects on spectra of molecular gases and their practical consequences,” *Journal of Quantitative Spectroscopy and Radiative Transfer*, vol. 213, pp. 178–227, Jul. 2018, doi: 10.1016/j.jqsrt.2018.03.016.
- [45] D. Jacquemart, R. Gamache, and L. S. Rothman, “Semi-empirical calculation of air-broadened half-widths and air pressure-induced frequency shifts of water-vapor absorption lines,” *Journal of Quantitative Spectroscopy and Radiative Transfer*, vol. 96, no. 2, Art. no. 2, Dec. 2005, doi: 10.1016/j.jqsrt.2004.11.018.
- [46] D. Robert and J. Bonamy, “Short range force effects in semiclassical molecular line broadening calculations,” *J. Phys. France*, vol. 40, no. 10, pp. 923–943, 1979, doi: 10.1051/jphys:019790040010092300.

- [47] R. A. Toth, "Linelists of water vapor parameters from 500 to 8000 cm^{-1} ," see <http://mark4sun.jpl.nasa.gov/h2o.html>, Apr. 2014, Accessed: Apr. 18, 2014. [Online]. Available: <http://mark4sun.jpl.nasa.gov/data/spec/H2O/paperh2o.pdf>
- [48] R. A. Toth, "Measurements and analysis (using empirical functions for widths) of air- and self-broadening parameters of," *Journal of Quantitative Spectroscopy and Radiative Transfer*, vol. 94, no. 1, pp. 1–50, Aug. 2005, doi: 10.1016/j.jqsrt.2004.08.041.
- [49] M. Birk and G. Wagner, "Temperature-dependent air broadening of water in the 1250–1750 cm^{-1} range," *Journal of Quantitative Spectroscopy and Radiative Transfer*, vol. 113, no. 11, pp. 889–928, Jul. 2012, doi: 10.1016/j.jqsrt.2011.12.013.
- [50] D. Priem, F. Rohart, J.-M. Colmont, G. Wlodarczak, and J.-P. Bouanich, "Lineshape study of the $J=3\leftarrow 2$ rotational transition of CO perturbed by N_2 and O_2 ," *Journal of Molecular Structure*, vol. 517, pp. 435–454, Feb. 2000, doi: 10.1016/S0022-2860(99)00268-9.
- [51] R. R. Gamache, E. Arié, C. Boursier, and J.-M. Hartmann, "Pressure-broadening and pressure-shifting of spectral lines of ozone," *Spectrochimica Acta Part A: Molecular and Biomolecular Spectroscopy*, vol. 54, no. 1, pp. 35–63, Jan. 1998, doi: 10.1016/S1386-1425(97)00202-3.
- [52] D. Forthomme, M. J. Cich, S. Twagirayezu, G. E. Hall, and T. J. Sears, "Application of the Hartmann–Tran profile to precise experimental data sets of $^{12}\text{C}_2\text{H}_2$," *Journal of Quantitative Spectroscopy and Radiative Transfer*, vol. 165, pp. 28–37, Nov. 2015, doi: 10.1016/j.jqsrt.2015.06.013.
- [53] M. J. Cich *et al.*, "Temperature-Dependent, Nitrogen-Perturbed Line Shape Measurements in the $\nu_1 + \nu_3$ Band of Acetylene Using a Diode Laser Referenced to a Frequency Comb," *J. Phys. Chem. A*, vol. 117, no. 50, pp. 13908–13918, Dec. 2013, doi: 10.1021/jp408960e.
- [54] J. S. Wilzewski, M. Birk, J. Loos, and G. Wagner, "Temperature-dependence laws of absorption line shape parameters of the $\text{CO}_2 \nu_3$ band," *Journal of Quantitative Spectroscopy and Radiative Transfer*, vol. 206, pp. 296–305, Feb. 2018, doi: 10.1016/j.jqsrt.2017.11.021.
- [55] B. Vispoel, J. H. Cavalcanti, E. T. Paige, and R. R. Gamache, "Vibrational dependence, temperature dependence, and prediction of line shape parameters for the $\text{H}_2\text{O}-\text{N}_2$ collision system," *Journal of Quantitative Spectroscopy and Radiative Transfer*, vol. 253, p. 107030, Sep. 2020, doi: 10.1016/j.jqsrt.2020.107030.
- [56] B. Vispoel, J. H. Cavalcanti, and R. R. Gamache, "Modified complex Robert-Bonamy calculations of line shape parameters and their temperature dependence for water vapor in collision with N_2 ," *Journal of Quantitative Spectroscopy and Radiative Transfer*, vol. 228, pp. 79–89, May 2019, doi: 10.1016/j.jqsrt.2019.02.023.